Spectral optical vortex modulation from geometric phase diamond metasurface arrays

Mikaël Ghadimi Nassiri, Gediminas Seniutinas, Christian David, Saulius Juodkazis, Etienne Brasselet

Applied Physics Letters ARTICLE scitation.org/journal/apl

Spectral optical vortex modulation from geometric phase diamond metasurface arrays

Cite as: Appl. Phys. Lett. **118**, 201104 (2021); doi: 10.1063/5.0048999
Submitted: 28 February 2021 · Accepted: 30 April 2021 ·
Published Online: 18 May 2021

Mikaël Ghadimi Nassiri,[1] Gediminas Seniutinas,[2] Christian David,[2] Saulius Juodkazis,[3] and Etienne Brasselet[1,a)]

AFFILIATIONS

[1]University Bordeaux, CNRS, LOMA, UMR 5798, Talence, France
[2]Paul Scherrer Institute, CH-5232 Villigen-PSI, Switzerland
[3]Optical Sciences Center and ARC Training Centre in Surface Engineering for Advanced Materials (SEAM), Faculty of Science, Engineering, and Technology, Swinburne University of Technology, Hawthorn, Victoria 3122, Australia

[a)]**Author to whom correspondence should be addressed:** etienne.brasselet@u-bordeaux.fr

ABSTRACT

Agile management of the optical orbital angular momentum encompasses temporal, spatial, and spectral aspects that, once combined, offer new perspectives in our way to manipulate light. To date the spectral control is mainly limited to tunable operating wavelength and polychromatic capabilities. Recently, a multispectral approach has been proposed [Phys. Rev. Lett. **121**, 213901 (2018)] to achieve independent orbital angular momentum state control on multiple spectral channels. Here we report on the design, fabrication and implementation of a solid-state multispectral approach that consists of arrays of optical diamond micro-metasurfaces. Obtained device exhibits superior performances with respect to the original attempt, both regarding the spectral vortex purity, the ability to deal with high photon flux, and the orbital angular momentum diversity across the spectrum. These results motivate further development of metasurface-based integrated spin–orbit photonics technologies.

Manipulating the spatial degrees of freedom of light is a routine optical process achieved by the so-called spatial light modulators, which goes beyond bespoke use in research laboratories. Indeed, spatial light modulators have become essential in many technologies such as laser 3D printing, ultrafast pulse shaping, optical holography, optical manipulation, optical computing, or optical imaging. The basic idea is to impart independently controllable local changes of either polarization state, phase, intensity, or propagation direction to an incident light field. In the framework of the present work devoted to the management of optical orbital angular momentum, here we deal with imparting azimuthally varying phase profiles to an incident Gaussian beam. This is customarily achieved in a flexible way in time, space, and wavelength by using programmable liquid crystal spatial light modulators that provide uniform phase control at the pixel scale.

Still, managing the wavelength-dependent orbital angular momentum state of a polychromatic light beam remains a difficult task that attracts recent interest under various perspectives (optical imaging, optical manipulation, ultrafast laser physics, structured light-matter interactions), see for instance.[1–6] In particular, it has been proposed to use arrays of non-uniform pixels, each of them acting as a spin–orbit geometric phase spatial light modulator endowed with vortex shaping functionality for a given wavelength.[3] By doing so, multispectral management of the photon orbital angular momentum has been experimentally reported, however, with some limitations inherent to the use of localized liquid crystal umbilical defects. Namely, (i) the integer topological charge ℓ of the set of the generated quasi-monochromatic vortex fields, which refers to a field amplitude proportional to $\exp(i\ell\phi)$ where ϕ is the azimuthal angle in the transverse plane with respect to the propagation direction of light, is restricted to the value $|\ell| = 2$; (ii) the purity parameter η, which refers to the power fraction of the output field that experiences the phase shaping, is limited to the range $0.8 < \eta < 0.95$ in the explored visible spectral range with less than 200 nm extent; (iii) there is a variability of the singular phase mask centering with respect to the pixel; (iv) the device is limited to the use of low-level optical intensities. Here we solve all these issues by using a highly transparent solid-state approach that consists of arrays of topological pixels made from diamond micro-metasurfaces, thus enriching diamond optics and photonics[7] with a new twist.

In our experiments, we choose a subwavelength grating design according to Ref. 8. The difference with the latter artificial space-variant birefringence approach, where the in-plane orientation angle ψ

of the grating wavevector—that is the effective optical axis—varies continuously with ϕ according to $\psi = q\phi$ with q integer or half-integer, is that we use a piecewise version of it. Specifically, we use a $16|q|$-sector design similar to that used in Ref. 9, where ψ varies by $\pi/8$ step between two adjacent sectors. A structural design of order q is intended to produce an optical vortices with topological charge $\ell = \pm 2q$ owing to the spin–orbit interaction of light.[10] Indeed, once irradiated by a circularly polarized light beam with helicity $\sigma = \pm 1$, which refers to the circular polarization handedness, the contra-circularly polarized light emerging from a structure characterized by ψ acquires a pure phase term $\exp(2i\sigma\psi)$ of a geometric nature. Topological metapixels having 100 μm diameter and 200 nm grating period are made out of polycrystalline chemical vapor deposited diamond. We note that the proposed approach generalizes previous realizations of geometric phase diamond metasurfaces, so far restricted to $|\ell| = 2$[11] in the infrared domain, to arbitrary values of topological charges in the visible domain as recently anticipated.[12]

The metapixels are fabricated from 10 μm thick diamond membranes supported by a silicon frame supplied by Diamond Materials GmbH and the main steps are summarized in what follows. At first, the membranes are cleaned in H_2SO_4:H_2O_2 2:1 solution at 120 °C to remove organic contamination. Then, the membranes are sputter-coated with 10 nm thick Cr layer and subsequently spin-coated with ~500 nm thick negative tone resist FOX16. The resist is patterned in electron beam lithography system Raith EBPG 5000PlusES using 100 keV electron energy. After the exposure, the samples are developed for 5 min in Microposit 351:H_2O 1:3 solution at room temperature, then thoroughly rinsed in de-ionized water and isopropanol. The unmasked part of the Cr layer is removed in a Cl_2/O_2-based plasma etching step revealing the underlying diamond for subsequent etching. Finally, the resist pattern is transferred into diamond by oxygen plasma etching in Oxford PlasmaLab 100 with the following etching parameters: chamber pressure of 1.3 Pa, 30 $cm^3 min^{-1}$ O_2 flow rate, powers of inductively coupled plasma and radio frequency are 750 W and 100 W, respectively. After diamond etching, the remaining resist mask is stripped in 10% HF solution and the samples are cleaned in Cr etchant and H_2SO_4:H_2O_2 2:1 solution, followed by rinsing in de-ionized water and isopropanol, leaving the structures ready for immediate use.

A typical metapixel with $q = 1$ is shown in Fig. 1(a) and successive enlargements displayed in panels (b) and (c) allow appreciating finer details and structural quality. Note a disk shaped central area with 1 μm radius is purposely left unstructured for practical reasons. The etching depth $h \simeq 800$ nm, the fraction $F \simeq 0.65$ of the grating period that is filled with diamond, and electron beam exposure dose of 7500 $\mu C\,cm^{-2}$ are chosen in order to optimize the purity parameter over the whole visible domain. The overall purity performance of seven distinct metapixels enabling the generation of optical vortices with topological charge $1 \leq |\ell| \leq 7$ in the visible domain is summarized in Fig. 1(d). The measurement consists in acquiring the transmission spectra $T^{(\pm\sigma)}(\lambda)$ of the $\pm\sigma$-polarized output components for an incident σ-polarized Gaussian beam with 56 μm diameter centered on the metapixel, from which $\eta = T^{(-\sigma)}/(T^{(\sigma)} + T^{(-\sigma)})$ is evaluated. We obtain $0.9 < \eta < 0.99$ over the spectral range 430 nm $< \lambda <$ 800 nm. This outperforms previous polychromatic features[3] while not requiring to adapt the fabrication parameter to the considered multispectral field made of a superposition of N distinct spectral channels. In fact the latter ultra-broadband feature results from the trapezoidal-like rather than square-shaped grating profile [see Fig. 1(c)], which is a known asset of diamond subwavelength gratings optics already exploited for infrared high-contrast astronomical imaging.[13]

Our approach relies on the spatial arrangement of above-mentioned seven metapixels into one dimensional arrays on the diamond membrane, as shown in Fig. 2. In this figure, both the piecewise space-variant birefringent design and the optical vortex generation are assessed by optical means in panel (a) and (b), respectively. Note that these measurements, as well as others, are all made by placing the suspended membrane on a glass coverslip in order to ease the handling of the sample. The spectral on-axis total transmission losses of the structures are also evaluated by using on-axis $\simeq 60$ μm diameter incident Gaussian beam and measuring the transmission as a function of q at $\lambda_0 = 532$ nm [see Fig. 3(a)]. The decrease in the transmission as q increases finds its origin in the sectors' selvedge that diffracts light [see Fig. 3(b)], which in turn reduces the effective cross section of the

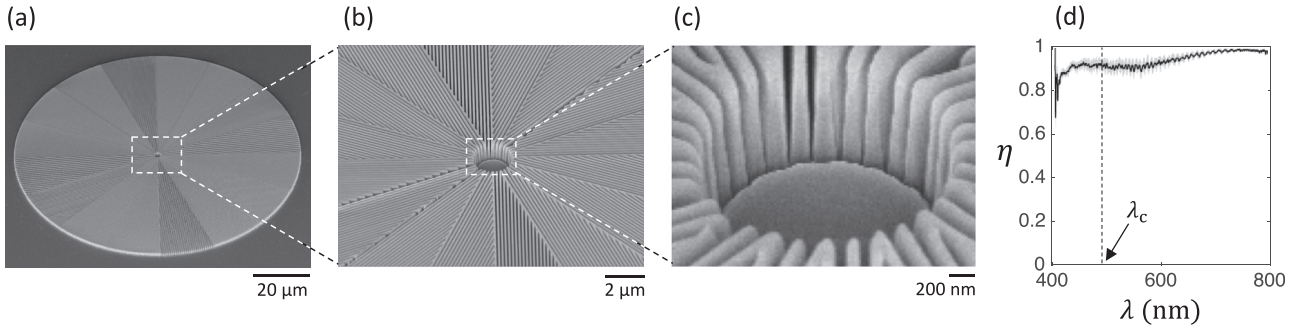

FIG. 1. (a) Scanning electron microscopy (SEM) image of a 100 μm diameter diamond metasurface pixel associated with $q = 1$. (b) Enlargement of the panel (a) illustrating the 16-sector space-variant subwavelength grating design. (c) Enlargement of the panel (b) showing the trapezoidal-like profile of the nanogratings. (d) Purity parameter as a function of wavelength in the visible domain. The solid line refers to the average value $\langle\eta\rangle$ over a set of seven pixels associated with $q = \left(\frac{1}{2}, 1, \frac{3}{2}, 2, \frac{5}{2}, 3, \frac{7}{2}\right)$ and the gray area refers to values ranging between $\langle\eta\rangle \pm \mathrm{std}(\eta)$ where "std" refers to standard deviation. Note that data variability at shorter wavelengths is due to the fact that the used supercontinuum source barely emits around 400 nm, which leads to substantial signal-to-noise ratio, and we note that the zeroth-order diffraction condition fails below $\lambda_c \simeq 490$ nm for the used 200 nm grating period.

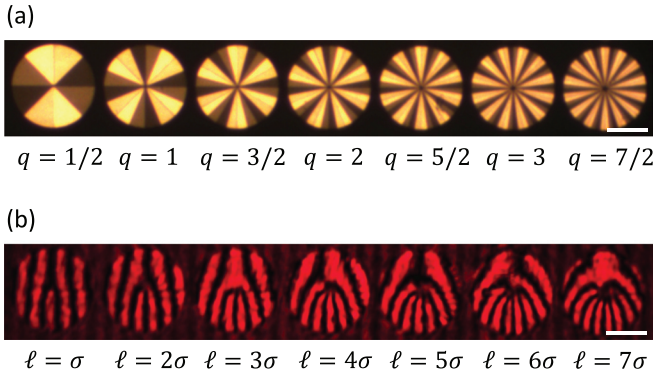

FIG. 2. (a) Natural white light imaging of an array of seven metapixels with increasing values of q placed between crossed linear polarizers. (b) Interferometric characterization of the vortex beam shaping at 633 nm wavelength using σ-polarized incident field and $-\sigma$-polarized reference field. The orientation of the forks is flipped upside down by the operation $\sigma \rightarrow -\sigma$. Scale bars: 50 μm.

incident beam. This is supported by modeling the latter losses by null transmission through a set of $16q$ radial segments with width e, as illustrated in the inset of Fig. 3(a). Taking e as an adjustable parameter, we obtain $e \simeq 590$ nm, which fairly agrees with direct SEM observations shown in Fig. 3(b).

Spectral modulation of the orbital angular momentum is then implemented according to a dispersion/recollimation experimental scheme depicted in Figs. 4(a) and 4(b). The idea consists to disperse an incident polychromatic field made of a supercontinuum laser source and to recollimate it onto an array of multimode optical fibers that define the spectral channels as done in Ref. 3. Note that here we provide undisclosed yet details of the setup allowing to readily reproduce the experiment, see the caption of Fig. 4. In addition, the spectral characterization of the multispectral light at the output of the optical fiber array is shown in Fig. 4(d). A Gaussian amplitude mask is placed at ~12 cm from the output of the optical fiber array that is reimaged

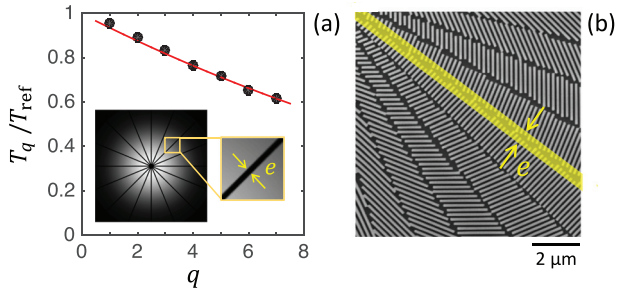

FIG. 3. (a) On-axis total transmission T_q as a function of the structural order q normalized to the unstructured membrane transmission T_{ref}, at 532 nm wavelength. Filled markers: experimental data. Solid line: best fit adjustment of the model (see the text) and its corresponding guide for the eye. Inset: illustration of the cross section reduction of the $\simeq 60$ μm-diameter incident Gaussian beam assuming null transmission through 16 inter-sector radial segments with width e for $q = 1$. (b) Local SEM image of a metapixel with $q = 7/2$ providing a detailed view of the sectors' selvedge that leads to diffraction losses. The value $e \simeq 590$ nm of the width of the modeled segment-like selvedge that corresponds to the best fit in panel (a) is depicted on scale by a yellowed segment.

on the metapixel array using an objective lens that gives a Gaussian beam diameter of $\simeq 60$ μm for each spectral channel, which guarantees that the optical field is processed in its entirety. The dispersed multispectral field in the plane of the metapixel array is shown in Fig. 5(b) when observed between crossed linear polarizers. As propagation further takes place, every spectral component is shaped into a donut intensity profile independently of the incident polarization state in the limit of $\eta \rightarrow 1$ [see Fig. 5(c) in the case of incident σ-polarized light]. When considering the whole multispectral field, one gets a radial rainbow associated with wavelength-dependent photon orbital angular momentum state, as shown in the left panel of Fig. 5(d). As such, the latter rainbow strongly differs from previously reported ones made of polychromatic vortex field generated by spin–orbit interaction wavelength-dependent optical anisotropy, see for instance,[14] for which the orbital state is wavelength-independent. When the incident light

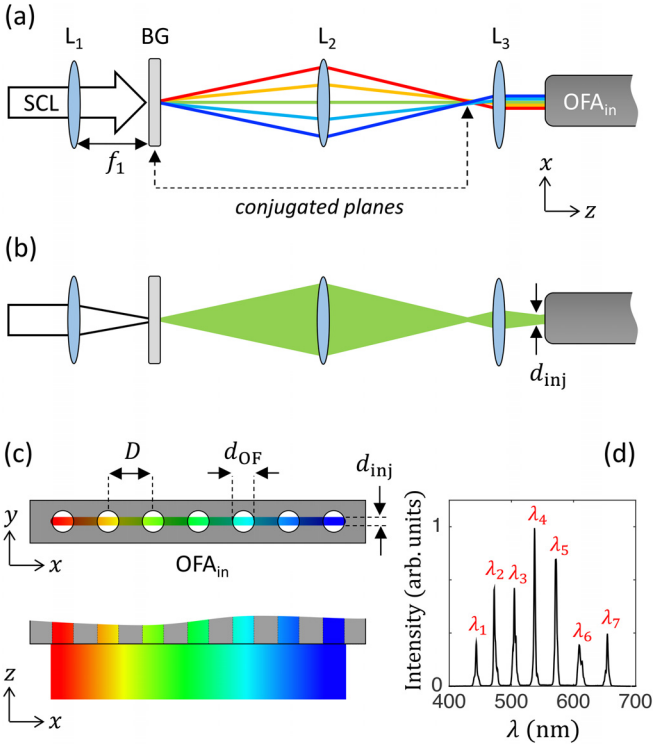

FIG. 4. (a) Ray-optics sketch illustrating the dispersion/recollimation scheme used to prepare a discrete set of seven spectral channels out of a supercontinuum laser using an optical fiber array. Note: here we depict the grating as a transmission grating, though the used one is a blazed reflection grating (GR13-0605 from Thorlabs). SCL: supercontinuum laser; BG: blazed grating; L_1: lens with focal length $f_1 = 50$ mm; L_2: achromatic doublet lens with focal length $f_2 = 75$ mm; L_3: in practice, a concave mirror (CM254-025-E02 from Thorlabs) with focal length $f_2 = 25$ mm; OFA_{in}: input of the optical fiber array. (b) Beam-optics counterpart of panel (a) for a given spectral channel (here the on-axis one). This emphasizes the Gaussian beam propagation and shows the diameter $d_{\mathrm{inj}} \simeq 50$ μm of every Gaussian spectral channel injected at normal incidence on an individual optical fiber at the entrance of OFA_{in}. (c) Sketch of the input facet of the OFA, that is charecterized by a fiber interdistance $D = 250$ μm and an optical fiber diameter $d_{\mathrm{OF}} = 125$ μm with a 50 μm core diameter. (d) Typical spectrum measured at ~5 cm from the output of the OFA with a fiber-spectrometer having an input fiber diameter of 200 μm.

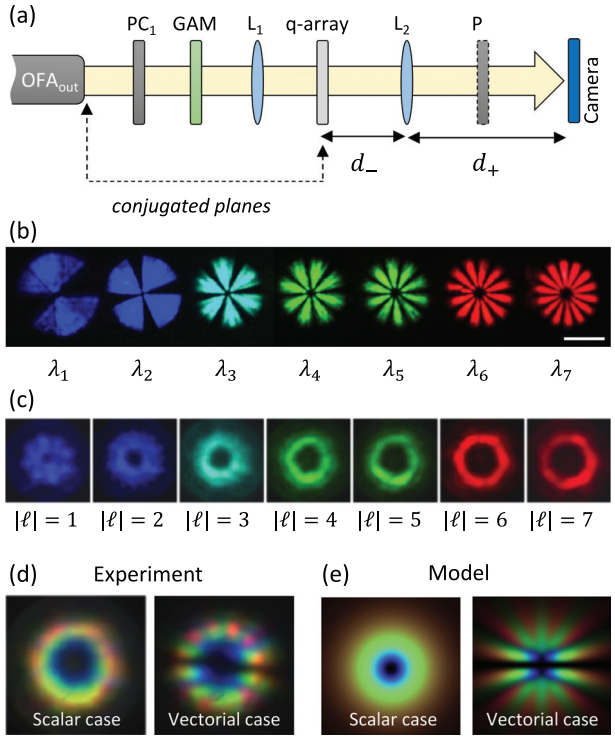

FIG. 5. (a) Sketch of the setup enabling multispectral optical vortex modulation. OFA_{out}: output of the optical fiber array; PC_1: polarization controller; P: linear polarizer that is placed or removed depending on the observations; GAM: reflective Gaussian amplitude mask (NDYR20A from Thorlabs); L_1: 4× objective lens with numerical aperture NA = 0.1; q-array: array of metapixels; L_2: 4× objective lens with NA = 0.1 and effective focal length $f_2 = 45$ mm. (b) Image of the metapixel array observed between crossed linear polarizers, setting $1/d_- + 1/d_+ = 1/f_2$. The brightness of the channels 1, 2, 3 and 7 is enhanced to ease the visual inspection. Scale bar: 50 μm. (c) Far field total intensity profiles of the seven individual spectral channels with wavelength $\lambda_{n=1to7}$ for an incident σ-polarized light, setting $d_- = d_+ = f_2$. Each spectral channel is individually selected by adjusting the transverse position of an iris placed after the lens L_2 shown in Fig. 4(a). [(d) and (e)] Far field intensity profiles of the multispectral field with spectrally modulated orbital angular momentum states. Left panels (scalar case): total field with σ-polarized incident field; Right panels (vectorial case): field observed between crossed linear polarizers.

field is linearly polarized, one obtains a multispectral superposition of vector beams with wavelength-dependent order. This is illustrated in the right panel of Fig. 5(d) where an output linear polarizer is placed, which leads to the appearance of a two-dimensional inhomogeneous multicolor intensity pattern. These far field observations are qualitatively compared with calculations by assuming that every metapixel imparts a continuous helical phase to the incident field. Namely, we calculate the *ad hoc* intensity profiles $I_{\text{scalar}} \propto \sum_{n=1to7} |\mathcal{F}_n[E_0^{(n)} \exp(-r^2/w^2 + in\phi)]|^2$ and $I_{\text{vectorial}} \propto \sum_{n=1to7} \sin^2(n\phi)|\mathcal{F}_n[E_0^{(n)} \exp(-r^2/w^2 + in\phi)]|^2$, where $\mathcal{F}_n$ refers to the spatial Fourier transform for the wavelength λ_n and where the prefactors $E_0^{(n)}$ are chosen for the sake of a visual comparison with experiments. Obviously, the discrepancies between the experimental observations and the latter qualitative attempt to describe the observations call for developing a proper theoretical treatment of spectral optical vortex modulation. Still, the present results propose an experimental pathway to explore new horizons for both scalar and vectorial field polychromatic structuring in the optical domain, which motivates continued interest as illustrated by recent theoretical results about 3D topological polarization structuring of polychromatic waves.[15]

Summarizing, we have proposed a robust solid-state approach to the multispectral management of the photon orbital angular momentum by means of metapixel arrays, where every metapixel is a microscopic geometric phase diamond metasurface. By doing so, one can obtain user-defined polarization-controlled multispectral superposition of orbital angular momentum states $\{\pm\ell(\lambda_i)\}$ over a multispectral light field $\{\lambda_i\}$. Experimental results have been reported in the visible domain and can be readily extended to the infrared domain, for which diamond material suits well. The present approach offers an alternative option to a recent proposal based on geometric phase pixels made out liquid crystal topological defects[3] that could sustain high photon flux. It, thus, contributes to the emergence of novel experimental methods to achieve spatiotemporal couplings in extreme optical regimes while only a few proposals have been made to date, such as those relying on either linear[2] or nonlinear optical processes.[4] Other kinds of recently unveiled spatiotemporal optical vortices associated with transverse orbital angular momentum[16] might also benefit from such developments.

Authors thank the financial support of Initiative of Excellence of the University of Bordeaux (ANR-10-IDEX-03–02) and Conseil Régional de Nouvelle Aquitaine (project HELIXOPTICS).

DATA AVAILABILITY

The data that support the findings of this study are available from the corresponding author upon reasonable request.

REFERENCES

[1]L. Yan, P. Gregg, E. Karimi, A. Rubano, L. Marrucci, R. Boyd, and S. Ramachandran, "Q-plate enabled spectrally diverse orbital-angular-momentum conversion for stimulated emission depletion microscopy," Optica **2**, 900–903 (2015).
[2]G. Pariente and F. Quéré, "Spatio-temporal light springs: Extended encoding of orbital angular momentum in ultrashort pulses," Opt. Lett. **40**, 2037–2040 (2015).
[3]M. Ghadimi Nassiri and E. Brasselet, "Multispectral management of the photon orbital angular momentum," Phys. Rev. Lett. **121**, 213901 (2018).
[4]L. Rego, K. M. Dorney, N. J. Brooks, Q. L. Nguyen, C.-T. Liao, J. San Román, D. E. Couch, A. Liu, E. Pisanty, M. Lewenstein, L. Plaja, H. C. Kapteyn, M. M. Murnane, and C. Hernández-García, "Generation of extreme-ultraviolet beams with time-varying orbital angular momentum," Science **364**, eaaw9486 (2019).
[5]A. H. Dorrah, M. Zamboni-Rached, and M. Mojahedi, "Wavelength and topological charge management along the axis of propagation of multichromatic non-diffracting beams," J. Opt. Soc. Am. B **36**, 1867–1872 (2019).
[6]S. N. Khonina, V. V. Podlipnov, S. V. Karpeev, A. V. Ustinov, S. G. Volotovsky, and S. V. Ganchevskaya, "Spectral control of the orbital angular momentum of a laser beam based on 3d properties of spiral phase plates fabricated for an infrared wavelength," Opt. Express **28**, 18407–18417 (2020).
[7]I. Aharonovich, A. D. Greentree, and S. Prawer, "Diamond photonics," Nat. Photonics **5**, 397–405 (2011).
[8]G. Biener, A. Niv, V. Kleiner, and E. Hasman, "Formation of helical beams by use of pancharatnam-berry phase optical elements," Opt. Lett. **27**, 1875 (2002).
[9]D. Hakobyan, H. Magallanes, G. Seniutinas, S. Juodkazis, and E. Brasselet, "Tailoring orbital angular momentum of light in the visible domain with metallic metasurfaces," Adv. Opt. Mater. **4**, 306–312 (2016).

[10]L. Marrucci, C. Manzo, and D. Paparo, "Optical spin-to-orbital angular momentum conversion in inhomogeneous anisotropic media," Phys. Rev. Lett. **96**, 163905 (2006).
[11]P. Forsberg, E. Vargas, C. Delacroix, O. Absil, B. Carlomagno, D. Mawet, S. Habraken, J. Surdej, and M. Karlsson, "Realizing the diamond annular groove phase masks for the mid infrared region: Five years of successful process development of diamond plasma etching," SPIE Proc. **9151**, 915119 (2014).
[12]G. Seniutinas, E. Brasselet, A. Balčytis, C. David, and S. Juodkazis, "Diamond: A gem for micro-optics," Mater. Today **21**, 798–799 (2018).
[13]E. Vargas Catalán, E. Huby, P. Forsberg, A. Jolivet, P. Baudoz, B. Carlomagno, C. Delacroix, S. Habraken, D. Mawet, J. Surdej, O. Absil, and M. Karlsson, "Optimizing the subwavelength grating of l-band annular groove phase masks for high coronagraphic performance," Astron. Astrophys. **595**, A127 (2016).
[14]E. Brasselet, Y. Izdebskaya, V. Shvedov, A. S. Desyatnikov, W. Krolikowski, and Y. S. Kivshar, "Dynamics of optical spin-orbit coupling in uniaxial crystals," Opt. Lett. **34**, 1021–1023 (2009).
[15]D. Sugic, M. R. Dennis, F. Nori, and K. Y. Bliokh, "Knotted polarizations and spin in three-dimensional polychromatic waves," Phys. Rev. Res. **2**, 042045 (2020).
[16]N. Jhajj, I. Larkin, E. W. Rosenthal, S. Zahedpour, J. K. Wahlstrand, and H. M. Milchberg, "Spatiotemporal optical vortices," Phys. Rev. X **6**, 031037 (2016).